Research Article Vol. 32, No. 8 / 8 Apr 2024 / Optics Express 13419
Optics EXPRESS

Time delay reservoir computing with a silicon microring resonator and a fiber-based optical feedback loop

GIOVANNI DONATI,[1,2,*] APOSTOLOS ARGYRIS,[1] MATTIA MANCINELLI,[2] CLAUDIO R. MIRASSO,[1] AND LORENZO PAVESI[2]

[1]Instituto de Física Interdisciplinar y Sistemas Complejos, IFISC (CSIC-UIB), Campus UIB, 07122 Palma de Mallorca, Spain
[2]Nanoscience Laboratory, Department of Physics, University of Trento, Via Sommarive 14, 38123 Trento, Italy
*giovanni.donati@strath.ac.uk

Abstract: Silicon microring resonators serve as critical components in integrated photonic neural network implementations, owing to their compact footprint, compatibility with CMOS technology, and passive nonlinear dynamics. Recent advancements have leveraged their filtering properties as weighting functions, and their nonlinear dynamics as activation functions with spiking capabilities. In this work, we investigate experimentally the linear and nonlinear dynamics of microring resonators for time delay reservoir computing, by introducing an external optical feedback loop. After effectively mitigating the impact of environmental noise on the fiber-based feedback phase dependencies, we evaluate the computational capacity of this system by assessing its performance across various benchmark tasks at a bit rate of few Mbps. We show that the additional memory provided by the optical feedback is necessary to achieve error-free operation in delayed-boolean tasks that require up to 3 bits of memory. In this case the microring was operated in the linear regime and the photodetection was the nonlinear activation function. We also show that the Santa Fe and Mackey Glass prediction tasks are solved when the microring nonlinearities are activated. Notably, our study reveals competitive outcomes even when employing only 7 virtual nodes within our photonic reservoir. Our findings illustrate the silicon microring's versatile performance in the presence of optical feedback, highlighting its ability to be tailored for various computing applications.

1. Introduction

In recent years, artificial neural networks have garnered significant attention for their remarkable ability to handle vast datasets and address complex tasks, such as facial and speech recognition, as well as time-series predictions [1]. These networks draw inspiration from their biological counterparts and fundamentally consist of artificial neurons interconnected with specific synaptic strengths. As the energy footprint of the training and operation of the digital neural networks has recently exponentially exploded [2], photonic hardware offers inherent advantages, including energy-efficient parallel processing at the speed of light, scalability, reduced susceptibility to noise, and the potential to overcome data transfer bottlenecks [3]. Remarkably, photonic neural networks have made significant strides in recent years, with notable advances in hardware implementations and network topologies [4]. Reservoir Computing (RC) is a popular hardware-friendly paradigm that makes the training of the neural network time- and cost-efficient [5,6]. In the RC concept, the reservoir is a set of interconnected, recurrent nonlinear nodes with fixed and untrained connectivities. A fixed relation between the input information and the reservoir is established, and only the output layer is trained by linear classifiers. Thus, any black box system with nonlinear dynamics suites the requisite of RC, resulting in a variety of physical implementations. The

#514617 https://doi.org/10.1364/OE.514617
Journal © 2024 Received 29 Nov 2023; revised 17 Feb 2024; accepted 19 Feb 2024; published 27 Mar 2024

Optics EXPRESS

reservoir nodes may refer to different pixels in a camera, which are connected by a tank of water where light has first propagated [7], or they may be even virtual when sampled in time from the dynamical response of only one physical node. The latter concept was proposed as time delay RC [8] and simplifies further the RC requisites by using only one physical nonlinear node - named real node - which is usually coupled to external feedback for introducing recurrence. Time delay RC allowed time-multiplexed networks with a large number of nodes, which could not be achieved otherwise [9]. Many optoelectronic and all-optical implementations have been proposed, including real nodes based on Mach Zehnder interferometers [10–13], semiconductor optical amplifiers [14], semiconductor ring lasers [15], semiconductor lasers [16–20] and VCSELs [21]. All these physical systems incorporate an external feedback loop to extend their memory and enrich their dynamic responses. The feedback may consist of an optical fiber or may be integrated on a chip [22,23]. An elegant implementation with just a simple and passive fiber loop, combined with photodetection nonlinearity, has been also proposed [24]. However, the coupling connection in a virtual reservoir does not necessarily require a feedback loop. It can also emerge from the inertia of the nonlinear phenomena within the real node itself, as recently demonstrated in single microring resonators [25,26].

In a recent work [27], we numerically investigated the behavior of a time delay RC system based on a single silicon microring resonator coupled to an optical feedback loop. The interest in silicon microrings is motivated by their compact footprint (down to μm size) and CMOS compatibility, along with their rich dynamical properties which enable key functions of biological neurons [28]. For example, the linear filtering properties of microrings, relying on their resonance nature, can emulate the input weights of photonic neurons [29–32]. Additionally, the nonlinearities induced in silicon microrings by two-photon absorption (TPA), allow threshold dynamics [26]. TPA nonlinear effects produce temperature and free carrier variations in the microring waveguide and thus result in an opposite refraction index change [33]. Thermal bistability [34] is achieved when thermal effects dominate over the free carrier ones and can emulate a sigmoid nonlinear function in a photonic neuron. Free carrier and temperature effects can compete to generate spiking output dynamics under a constant input optical signal, closely miming the spiking electrical activity of biological neurons [35–38].

In this study, we extend our preliminary numerical findings [27] by developing and deploying an experimental setup involving a single silicon microring resonator coupled with optical feedback, within a time delay reservoir computing (RC) model. Our experiments confirm both the microring and the external optical feedback as sources of memory in the system. We systematically evaluate the optimal system configuration for solving diverse benchmark computing tasks, encompassing Boolean operations, the Santa Fe prediction task, and the Mackey Glass prediction task. We find that the optical feedback is necessary to achieve error-free operation in delayed boolean tasks that require up to 3 bits of memory, while the microring nonlinearity is exploited to solve the Santa Fe and Mackey Glass prediction tasks. Remarkably, even with prediction tasks traditionally requiring a multitude of nodes, we demonstrate that a mere 7 virtual nodes in our photonic reservoir yield competitive outcomes. For the Santa Fe prediction task, the most optimal performance is obtained with 38 virtual nodes and the activation of microring's spiking dynamics, without relying on the feedback loop. In this case, we experimentally show that the spiking dynamics of the microring provides the long-term memory that is necessary to solve the task. To ensure the robust operation of our system and to counteract phase instabilities arising from environmental noise along the fiber-optic feedback loop, we incorporate a phase-locked loop electronic controller, which directly manages the phase state of the optical feedback.

The structure of this manuscript is as follows: Section 2 introduces the design and principles underpinning the time delay RC employing silicon microring resonators. Section 3 elaborates on the experimental setup and operational parameters. Section 4 presents and discusses the outcomes obtained in our system across various computing benchmark tasks. Finally, in Sections 5 and

Optics EXPRESS

6, we provide a comparative analysis with other photonic implementations and the concluding insights of this study.

2. Time delay RC with a microring resonator

In Fig. 1 we show the basic functionality of the time delay RC, employing a photonic reservoir. It consists of a microring resonator in add-drop filter configuration with an external optical feedback connectivity. The time delay RC model assumes that a time-multiplexed interpretation of the information to be processed is introduced at the input. Therefore, this scheme is optimal for processing time-dependent information. The input information to be processed (x_i) is amplitude-encoded in a sequence of optical pulses with a duration of b_w, separated in time by b_s, and represents the digital or analog values of the computational task. Therefore, the processing bit rate of the neural network is equal to $B_r = 1/(b_w + b_s)$. Before its encoding to the optical domain, each input value is masked with a random vector of values M between 0 and 1, that has a length equal to the number of virtual nodes N_v defined in the reservoir [8]. The duration of each mask value is equal to the temporal separation of the virtual nodes $\theta_v = b_w/N_v$. The mask pattern is repetitive for all encoded pulses and is encoded here offline. However, physical systems could be incorporated to create this pattern in an analog form [39,40].

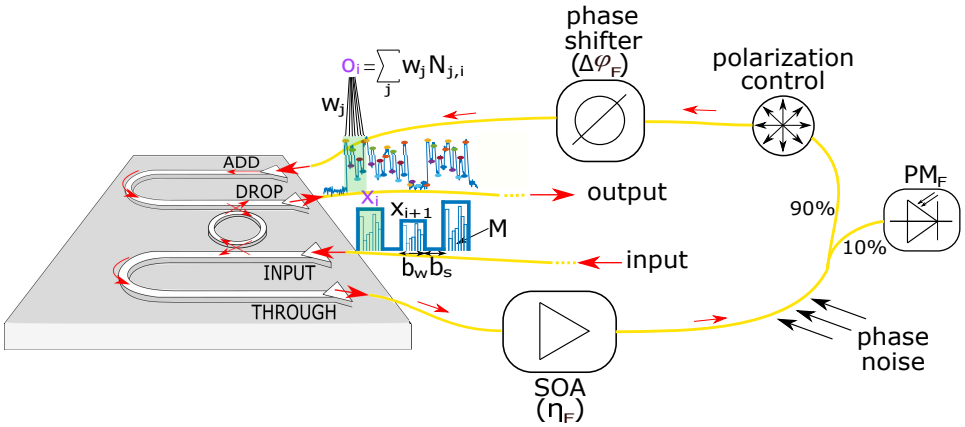

Fig. 1. Time delay RC based on microring resonator with external optical feedback. The microring is integrated in a silicon-on-insulator chip and accessed by a fiber array. The feedback delay line is realized externally, via a single-mode optical fiber. It includes a series of instruments that allow to control and monitor the phase ϕ_F, the strength η_F, and the polarization of the feedback signal.

The resulting masked optical information is introduced at the input port of the silicon microring resonator, while the photodetected signal at the drop port provides the responses of the virtual nodes sequentially. A linear, weighted combination of these responses within the duration b_w of an encoded piece of information x_i results in the predicted value o_i. The latter is computed as $o_i = \sum(w_j \cdot N_{j,i})$, with $N_{j,i}$ being the response of the virtual node j to the input i. w_j represents the output weights of the different virtual nodes that apply to the linear classifier and that are computed during the training phase. A linear regression algorithm minimizes the normalized mean square error (NMSE) between the predicted (o_i) and target (y_i) values of the processed task, defined as:

$$NMSE = \frac{\sum_i (o_i - y_i)^2}{N_d \sigma_y^2}, \tag{1}$$

Optics EXPRESS

where σ_y indicates the standard deviation of the target series, and N_d the dataset dimension. The lower the *NMSE* is, the better the system predicts the target series.

The feedback connectivity is physically provided by a fiber loop which connects the microring's through and add ports. To control the strength (η_F) and the phase (ϕ_F) of the feedback signal, a semiconductor optical amplifier (SOA) and a phase shifter are included in the fiber loop.

Multiple characteristic times are present in the dynamical operation of the microring resonator. The photon lifetime τ_{ph} (typically in the ps range) determines the speed at which light is coupled in and out of the microring cavity. In contrast, the free carrier lifetime τ_{fc} (typically in the ns or tens of ns range) and the thermal relaxation time τ_{th} (typically in the hundreds ns range) govern the free carrier and temperature nonlinear dynamics that generate from TPA-processes within the microring [33]. Thus, several possibilities emerge from these time scales that can trigger transient dynamical operations. The latter can be obtained by introducing masking sequences with appropriate timing. For example, the duration of each mask value can be set to $\theta_v < \tau_{ph}$ to introduce transient dynamics based on the photon lifetime, while stretching the optical bit x_i to $b_w \approx \tau_{fc}$, thus exciting an appreciable free carrier population and obtain the nonlinear transformation of x_i, as done in our previous work [27]. Otherwise, the duration of each mask value can be set as $\tau_{ph} < \theta_v < \tau_{fc}$ to generate transient dynamics based on the free carrier nonlinearity inertia, while setting $b_w > \tau_{fc}$ to obtain a nonlinear transformation shaped from the free carrier and eventually the thermal dynamics. In the present work, we will consider this last scenario.

2.1. Feedback echo memory

The presence of a feedback line provides the system with optical memory, which can be useful for computing memory-demanding tasks in a time delay RC scheme. This memory mechanism can be understood by introducing a test optical pulse at the microring input port (Fig. 2). In this consideration, the test pulse has a duration $\tau_{ph} << b_w << \tau_F$, where τ_F is the fiber loop transit time. Depending on the operating frequency detuning of the microring $\Delta\nu_s = \nu_p - \nu_0$, with ν_p and ν_0 being the optical input and the microring resonance frequencies, three possible operations exist:

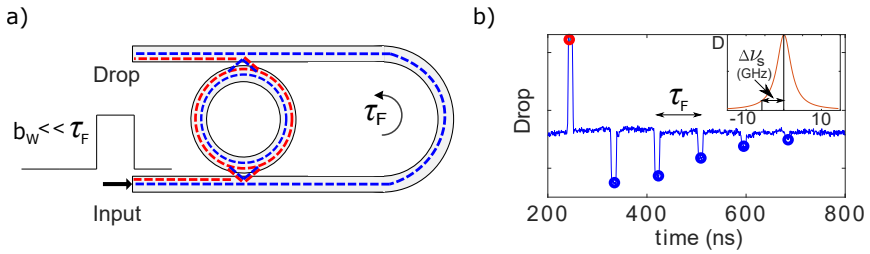

Fig. 2. Operation of a microring resonator coupled to an external optical feedback. a) An input optical pulse can be directly dropped by the microring resonator if $\Delta\nu_s = 0$ (red path), or it can iterate the microring-feedback loop system several times if $\Delta\nu_s \sim FWHM$ (blue path). b) Fading memory effect, when considering $\Delta\nu_s = 6$ GHz ($FWHM = 4.52$ GHz). The inset reports the drop transmission D, in the absence of feedback.

(i) $\Delta\nu_s = 0$: the optical input signal is resonant with the microring resonator and is ideally completely dropped (Fig. 2(a, red path)). In this case, the input pulse is directly transmitted to the drop port with 0.25 ps delay, which is our microring transit time.

(ii) $\Delta\nu_s >> FWHM$: the optical input signal is out of resonance and bypasses the microring propagating to the external feedback loop and then to the drop port. In this case, the system acts just as a delay line;

Optics EXPRESS

(iii) $\Delta\nu_s \sim FWHM$: the optical input signal is partially resonant. In this scenario, a fraction of the optical power is dropped following path (i), thus resulting in the first pulse detected in Fig. 2(b, red dot). The remaining optical power is transmitted to the through port and then coupled to the external feedback loop. It propagates along the fiber loop until reaching the add port, with a delay τ_F. At this point, the delayed signal is partially obtained at the drop port, thus generating the second detected pulse in Fig. 2(b, first blue dot). The rest is coupled back to the microring and then to the through port, thus reiterating the previous optical path. This results in a fading memory sequence of delayed pulses at the drop port separated by a time τ_F, which are indicated in Fig. 2(b, rest blue dots). The number of output pulse echoes obtained at the drop port, and thus the roundtrips that the optical pulse remains in the external loop depends on both $\Delta\nu_s$ and the amplification introduced in the external loop to reduce the losses. A maximum of five echoes were measured with our system when operating the systems with an amplification SOA gain of η_F=350 mA. Note that in real case scenarios, the condition i) ($\Delta\nu = 0$) is not completely satisfied, since part of the input signal is partially transmitted to the through port, following the microring's extinction ratio. However, this does not change the final performance, as this operating condition is not the optimal to solve the tasks that will be presented when using the feedback.

3. Experimental implementation

The configuration of the input layer, the real node, and the output layer of our experimental implementation are shown in Fig. 3. At the input layer, an optical carrier is generated by a CW tunable laser source (Pure Photonics) operating in C-band wavelengths. The optical carrier is amplitude-modulated with the input information using a Mach Zehnder modulator (MXAN-LN-10). The modulator is driven by a 500MHz arbitrary waveform generator (AWG, Teledyne model T3AFG500), and operated in the quadrature point using a bias controller (MBC-AN-LAB). The optical signal is amplified using an erbium-doped fiber amplifier (EDFA), while a variable optical attenuator (VOA) allows for tuning the input power before entering the reservoir. A polarization controller (PC) is used to match the TE polarization that is required by the microring resonator. Before entering the reservoir, 1 % of the signal is directed to a monitor detector PM_i, to measure the average input optical power.

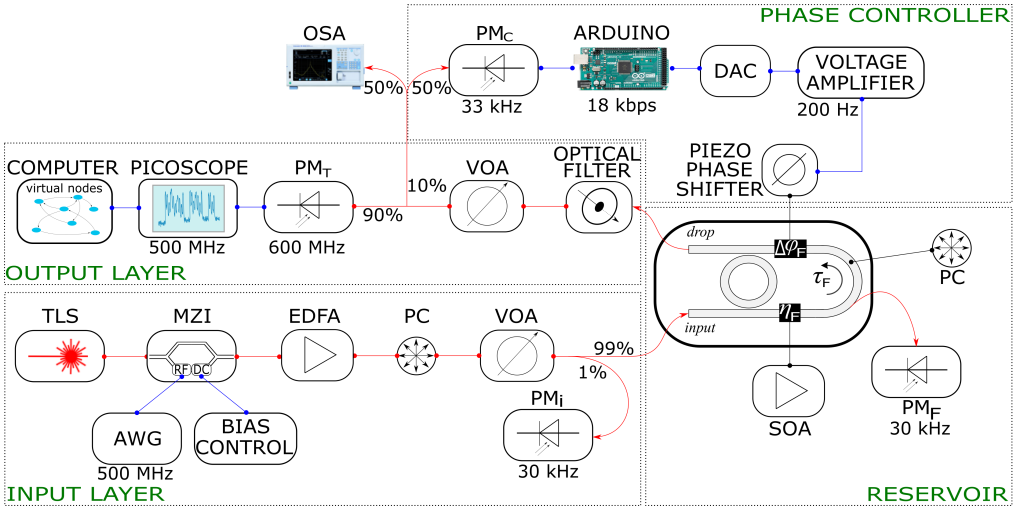

Fig. 3. Schematic of the experimental setup of time delay RC based on a microring resonator coupled to an external optical fiber loop. Red and blue lines correspond respectively to optical fiber and electrical connections.

Optics EXPRESS

The reservoir is based on a silicon microring resonator in an add-drop filter configuration fabricated on a SOI chip, coupled to an external optical fiber. The microring has a waveguide cross-section of 220×500 nm^2, a radius $r = 6.75$ μm, and equal gaps with the two bus waveguides of 238 nm. From its drop channel, we can measure its spectral profile and deduce a $FWHM = 4.52$ GHz ($FWHM = 36.4$ pm), and a quality factor $Q = 4.2 \times 10^4$, at a resonance cold position $\nu_0 = 193.16$ THz ($\lambda_0 = 1553.11$ nm). The four ports of the microring, as shown in Fig. 1, are accessible by grating couplers which are aligned and separated by 127 μm. An optical fiber-array made of 4 optical fibers is coupled to the 4 ports of the microring, with 5 dB optical losses per grating. The two fibers that are coupled to the microring's through and add ports are connected and act as an external optical feedback loop. An SOA (Thorlabs S7FC1013S), a piezo-driven phase shifter (Luna FPS-001), a polarizer and a photodetector (PM_F) are included in this fiber loop. With the latter, we monitor and ensure that the SOA always operates in a linear regime. The SOA controls the strength (η_F) of the feedback signal via partial compensation of the optical grating losses, and the phase shifter controls the phase (ϕ_F) of the feedback signal, two critical parameters for the reservoir operation [27]. The total transit time of the external loop is $\tau_F = 88ns$.

The drop port provides the dynamical response of the photonic reservoir to the output layer. The output signal is spectrally filtered to suppress the amplified spontaneous emission (ASE) noise of the SOA, while a second attenuation stage (VOA) ensures that the output optical power will not saturate the photodetection stage. 90% of the optical signal is photodetected (PM_t, Menlosystem, FPD610-FC-NIR, 600 MHz) and read out with an oscilloscope (Picoscope 6000, 500 MHz). The obtained values are stored and used for offline training and evaluation of the investigated tasks. The rest 10 % of the optical signal is used for optical monitoring (optical spectrum analyzer, OSA), but also for feeding a phase-locked loop controller that is used to stabilize the phase conditions within the feedback loop of the reservoir. For this operation, a slower photodetector (PM_c, Thorlabs, PDA10CS2, 3 KHz) is employed. However, the bandwidth of PM_c is fast enough to monitor environmental phase noise fluctuations but slow enough to filter out the input encoded information. In this way, the obtained electrical signal provides information regarding environmental phase noise and is fed to an electronic controller for its compensation. The controller includes an Arduino Mega, a voltage amplifier (200 Hz), and a piezo-driven fiber stretcher along the optical fiber loop. More information regarding the phase stabilization with this system is provided in the appendix. The microring stability was also ensured by automatizing the measures overnight, where the temperature in the lab and the mechanical vibrations of the optical table that holds the setup were minimal. The resonance position was continuously monitored, with fluctuations within 1 GHz during the entire night.

3.1. Operating configuration

The tested silicon microring can exhibit self-pulsation dynamics, a phenomenon that relies on free carrier concentration and temperature variations within the silicon waveguide [33]. To operate it in the linear regime, an input optical power around or below 100 μW has to be used. Higher optical power activates nonlinear dynamics, mainly affected by the free carrier dynamics and by self-pulsations. Our microring has a free carrier lifetime of $\tau_{fc} = 45$ ns, which is much higher than the typical one of a few ns reported in literature [33]. The photonic reservoir system is operated in the following way. The input information x_i is optically encoded in a sequence of masked pulses having a proportional amplitude, duration $b_w = 77$ ns, and zero separation time $b_s = 0$. Each optical pulse in this way has the necessary time to trigger a measurable free carrier variation within the microring waveguide ($b_w > \tau_{fc}$), and therefore is nonlinearly transformed by the internal microring dynamics. The mask values duration is set to $\theta_v = 11$ ns, and thus, $N_v = b_w/\theta_v = 7$ virtual nodes are defined within a duration of b_w. The feedback delay ($\tau_F = 88$ ns) is therefore larger than the optical input pulse duration ($b_w = 77$ ns) by one mask value

Optics EXPRESS

duration (θ_v = 11 ns), i.e. $\tau_F = b_w + k\theta_v$, with $k = 1$. This asynchronous encoding, initially proposed in [10], allows coupling every virtual node to a delayed state of the previous neighbor node, thus defining a ring topology connection which can turn out beneficial for computation [41]. In this work, the asynchronous encoding will be compared to the synchronous one, where the feedback delay is equal to the encoded pulse duration ($\tau_F = b_w^{'}$ = 88 ns), by defining an additional virtual node ($N_v^{'} = 8$). In parallel, another connectivity occurs in the reservoir whenever the TPA microring nonlinearities are activated. For the given θ_v, the mask modulation time $\theta_v \approx \tau_{fc}/4$, introduces nonlinear free carrier transients dynamics that couple neighboring virtual nodes.

4. Results

The computing capabilities of the investigated photonic reservoir are tested on different benchmark tasks, such as delayed boolean digital tasks and the Santa Fe and Mackey Glass analog prediction tasks. The dataset size for all tasks considered is $N_d = 4200$. The first 200 elements are used to drive the system in an operating regime, eliminating dependencies from the initial conditions. The next 3000 data samples are used to train the network and the rest 1000 data samples are used for testing the system on previously unseen entries. The linear classifier applied at the output of the analog hardware system uses a ridge regression parameter of 10^{-4}. We always provide the classifier with virtual node states that are sampled from only the present input bit response. This ensures that the memory acquired originates from the response of the physical system. Other approaches extend the sampling region of virtual nodes to previous bits responses, introducing external memory to the classifier which is not provided by the physical system [17,22,23]. Our approach reduces the size and therefore the latency of the classifier to provide the output result. Finally, the same mask vector M is used in all experiments unless the number of virtual nodes is varied.

We study the performance of the photonic system on the selected tasks, for different configurations, by tuning the critical operational parameters. These are: the initial frequency detuning between the optical carrier and the resonance frequency of the microring $\Delta\nu_s$, the average injected input optical power P_{in}, the feedback phase $\Delta\phi_F$ at the drop port that is tuned via the phase controller (see Appendix), and the feedback strength η_F that is controlled by the SOA current. The ensemble of the above parameters determines the optical power circulating within the microring and thus its way of operation, linear or nonlinear, as well as the optical memory provided by the external loop. The dynamical system response during a task is acquired three times for each system configuration that is studied, and the corresponding performances are then averaged.

4.1. Delayed-boolean tasks

In delayed binary tasks the encoded input information x_i consists of a pseudo-random binary sequence (PRBS) of bits. The corresponding target sequence $y_i = B(x_i, x_{i-d})$ is the result of a generic boolean operation (B) on the current bit x_i and a previously encoded bit x_{i-d}, with $d \in Z_0^+$. The tasks we consider here are the standard AND, NAND, OR, and XOR logical operations reported in Table 1, including a memory capacity task (MC), which is defined as the capability of the system to recall the past bit value x_{i-d}. The value of d is a parameter that is varied to test the memory depth of the system. These operations are preliminary tasks that unveil some of the physics mechanisms of our photonic system. In particular, the XOR operation is in principle a difficult computational task, as it requires a nonlinear transformation to be solved [26].

Once the predicted values from o_i are computed, they are digitized to be compared with the digital target series y_i. To do so, the predicted values o_i are first normalized and then digitized according to a threshold comparator. The threshold value θ_{BER} is scanned in the range [0-1], with steps of 0.01, and the optimal chosen value minimizes the bit error rate (BER), defined as the ratio between the erroneously processed bits over the total number of bits.

Optics EXPRESS

Table 1. Delayed-boolean tasks operations between the actual bit x_i and a bit that has been previously seen by the network x_{i-d}.

x_i	x_{i-d}	MC y_i	AND y_i	NAND y_i	OR y_i	XOR y_i
0	0	0	0	1	0	0
0	1	1	0	1	1	1
1	0	0	0	1	1	1
1	1	1	1	0	1	0

The experiment is carried out for different system configurations. We use here an input average power equal to $P_{in} = 78$ μW. This value ensures that the microring operates in the linear regime, extending the linear memory of the system as shown in our previous work [27]. According to [42], a worse performance is expected when the microring operates in a nonlinear regime since it progressively distorts the iteration of the delayed information. We tune the strength of the optical feedback via the SOA current in its entire operating regime [0, 500] mA. The frequency detuning $\Delta\nu_s$ is studied in the range of $[-24, 24]$ GHz, which allows capturing the effects of the various dynamical regimes described in section 2.1. Finally, we study different phase conditions of the feedback loop $\Delta\phi_F$. For $\Delta\phi_F = \pi/6$ we obtain a constructive interference at the drop port, between the optical feedback signal and the internal microring optical signal. For $\Delta\phi_F = 5\pi/6$ we obtain a destructive interference (see Appendix).

In Fig. 4(a) we show the overall computing performance of the photonic reservoir for the boolean tasks and the memory capacity task described in Table 1, for different memory depths, from $d = 0$ up to $d = 10$. The provided BER values correspond to the lowest error obtained, after testing all possible parametrizations ($\Delta\nu_s$, η_F, $\Delta\phi_F$) of our system. From the performance of the MC task, we see that the reservoir can recall correctly up to two bits in the past, while the third bit ($d = 3$) can be recalled with a $BER \approx 0.04$. The boolean AND and NAND task results overlap completely, similarly to what was reported in [43]. They can be solved correctly up to $d = 3$. For $d = 4$, the obtained BER is 0.02. The OR and XOR tasks are solved correctly for up to two bits in the past. Figure 4(b) shows how the previous performance deteriorates when switching from an asynchronous to a synchronous encoding ($b_w = \tau_F = 88$ ns) with $N_v = 8$. As discussed in section 3.1, the ring connectivity of the asynchronous encoding is broken and the virtual nodes are no longer coupled within the reservoir. The only connectivity left is for each virtual node with its previous state, through the feedback loop.

By looking at the reservoir performance in the parameter space, it is possible to infer the reason behind the obtained best performance values shown in Fig. 4(a). Specifically, boolean tasks B and delay d combinations are shown in Fig. 5(a-d): MC0, XOR1, XOR2, and AND3, for their optimal feedback phases conditions $\Delta\phi_F$ which are indicated at the top of each panel. In the MC0 task (Fig. 5(a)), the target of the network is the input bit value x_i itself and is used as a "calibration" task. The input signal is partially transmitted to the drop port and provides the virtual nodes' response to the encoded information, while a delayed signal provided from the feedback is not necessary. We see in Fig. 5(a) that MC0 is solved for zero SOA current, which corresponds to a strongly attenuated external optical feedback, and for a wide range of $\Delta\nu_s$ around zero, where the input signal is mostly dropped. Configurations with even larger SOA currents also reach error-free operation, up to 350 mA. For even larger SOA current, lasing dynamics appear in the feedback loop due to the re-circulation of the optical signal by the microring. The lasing destroys the consistency required for computations. The rest of the tasks reported in Fig. 5(b-d) refer to $d \geq 1$, thus requiring memory of the previous information that can only be accessible through the feedback signal. As a result, the input optical signal needs to be slightly off-resonance to be

Optics EXPRESS

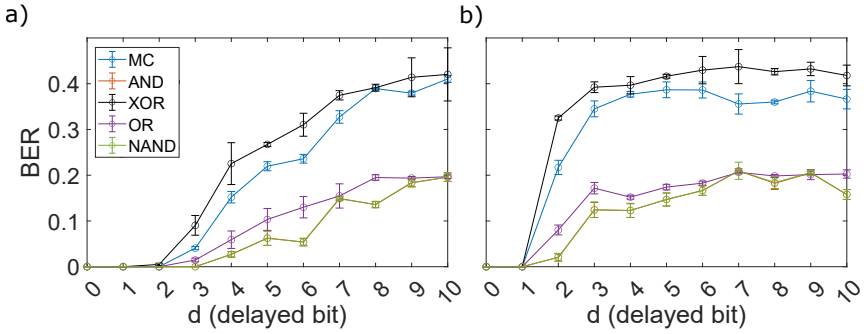

Fig. 4. Best BER obtained by the microring with feedback system in memory capacity and delayed boolean tasks $B(x_i, x_{i-d})$, for different memory length values d. a) Asynchronous processing schemes (k=1): $\theta_v = 11$ ns, $N_v = 7$, $\tau_F = 88$ ns, b) synchronous processing schemes (k=0): $\theta_v = 11$ ns, $N_v = 8$, $\tau_F = 88$ ns.

transmitted along the feedback loop, and the task is no more solved for $\Delta\nu_s = 0$. Still, the shift from resonance should not be too large and bypass the microring.

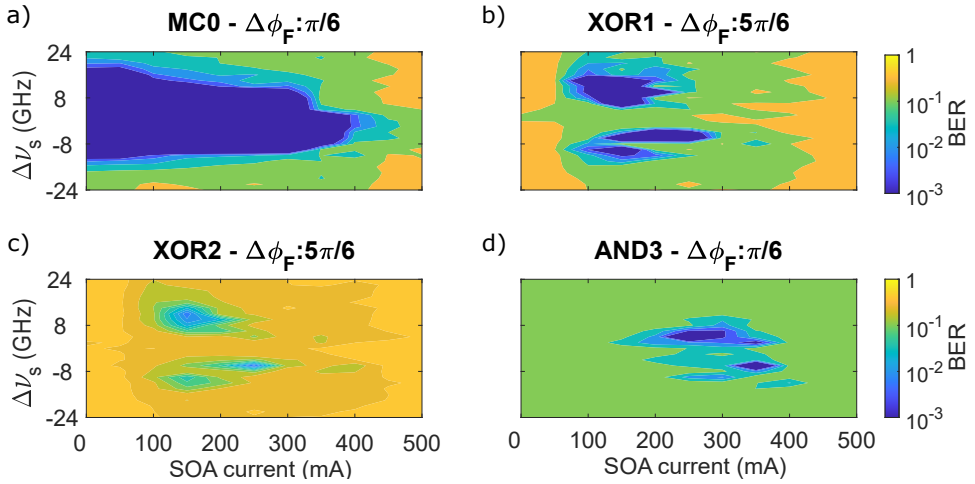

Fig. 5. Error rate performance for various memory capacity and boolean tasks: a) MC with $d = 0$, b) XOR with $d = 1$, c) XOR with $d = 2$, and d) AND with $d = 3$, in the $\Delta\nu_s$-SOA current parameter space, and for optimized $\Delta\phi_F$ values which are reported on top of each panel, using asynchronous encoding (k=1). $\theta_v = 11$ ns, $N_v = 7$, $\tau_F = 88$ ns. The type of the task is annotated by the acronym presented in Table 1, accompanied by the value of the length d.

The feedback phase $\Delta\phi_F$ is another important parameter. This is shown in Fig. 6, where the BER for the XOR1 and AND3 tasks are studied in the $\Delta\nu_s$-SOA current parameter space, for different $\Delta\phi_F$ values. Specifically, we show the results for $\Delta\phi_F = \pi/6$ (top panel), $\pi/2$ (middle panel), $5\pi/6$ (bottom panel). In the XOR1 task, the system exploits the destructive interference ($\Delta\phi_F = 5\pi/6$) between the direct drop transmission of the present bit $x_i = 1$ and the delayed information relative to the previous input bit $x_{i-1} = 1$ as provided by the feedback loop. This results in low output power at the drop port. Thus, the virtual node states corresponding to the XOR input combinations [1,1] and [0,0] are low in power and can be separated from the combinations [0,1] and [1,0]. Similarly, in the AND3 task (Fig. 6(b)), the system exploits the

Optics EXPRESS

constructive interference ($\Delta\phi_F = \pi/6$) between the drop response of the present input bit $x_i = 1$, and the delayed information relative to the previous input bit $x_{i-3} = 1$, to obtain the highest output power at the drop port. For all the other combinations of x_i and x_{i-3} the output power will be lower. The above attributes result in a final correct output classification.

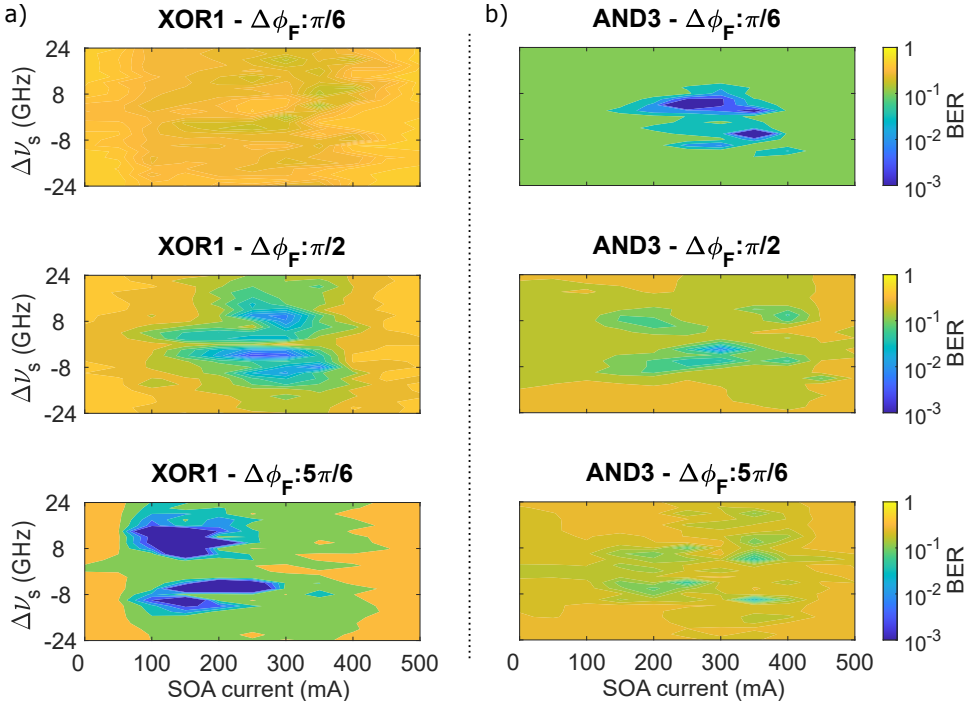

Fig. 6. Impact of the feedback phase $\Delta\phi_F$ on the a) XOR1 and b) AND3 delayed boolean task performance, for the $\Delta\nu_s$-SOA current parameter space. Constructive interference at the drop port is obtained for $\Delta\phi_F = \pi/6$, while destructive interference is obtained for $\Delta\phi_F = 5\pi/6$. Here, an asynchronous encoding (k=1) is used. $\theta_v = 11$ ns, $N_v = 7$, $\tau_F = 88ns$.

These results prove the importance of a proper feedback strength and interference condition at the drop port (through the $\Delta\phi_F$ parameter) for computing. When coupled to the linear microring regime, these conditions allow for useful echoes of the optical signal as a source of memory while exploiting the photodetection square law as the only nonlinearity of the system. Moreover, the use of a small number of virtual nodes is sufficient to account for up to 5 bits of memory. However, as it is known in reservoir computing, the increase in the dimensionality of the output for a given input is beneficial for computing tasks, including memory retrieval tasks. Thus, a higher number of virtual nodes is expected to slightly improve the performance. But, for a given sampling time between the virtual nodes, increasing their number will also reduce the computational speed of the reservoir. Under this compromise, it is common to minimize the number of virtual nodes needed down to a level that the reservoir provides an acceptable computing performance.

4.2. Prediction tasks

Other tasks may benefit from the microring's nonlinearity. Here, we discuss two examples. In the Santa Fe and Mackey Glass benchmark prediction tasks, the system is trained to predict future values x_{i+p} of the input series, from the current value x_i, with $p \geq 1$ indicating the number of steps ahead. The Santa Fe dataset is derived by experimental measures of the optical power

Optics EXPRESS

emitted by a far-infrared laser that operates in a chaotic regime [44], and is publicly available. The Mackey-Glass input series [45,46] is obtained by integrating in time the following equation:

$$\frac{dx(t)}{dt} = \frac{\alpha x(t-\tau)}{1+x(t-\tau)^{\beta}} - \gamma x(t), \tag{2}$$

with an integration step of 0.1, and the following parameter values: $\alpha = 0.2$, $\beta = 10$, $\gamma = 0.1$, and $\tau = 17$. The solution of Eq. (2) describes a weakly chaotic behavior, from which we apply an oversampling of a factor of 3 to make the task more difficult. The continuous range of values covered by the input series of both the Santa Fe and Mackey Glass tasks requires a linear encoding in the optical domain. To this aim, we reduce the AWG voltage to drive the MZ modulator in the linear regime of its transfer function.

The system is initially tested on these benchmark prediction tasks with the same asynchronous processing scheme described in section 3.1, incorporating only $N_v = 7$ virtual nodes. We scan the parameters $\Delta\nu_s$, η_F, $\Delta\phi_F$, and the input optical power P_{in} in a multidimensional setting to find the optimal system configuration for these tasks. We also restrict the frequency detuning to $\Delta\nu_s \in [-12, 12]$ GHz, excluding the conditions where $\Delta\nu_s >> FWHM$ in which the signal mostly bypasses the microring. The SOA current is evaluated in the range $[0, 500]$ mA, with steps of 100 mA, while the interference condition at the drop port is still tuned by the $\Delta\phi_F$ parameter. Finally, the input optical power is increased from 0.11 mW up to 1.5 mW. By doing so, we can operate the microring in a linear regime, for $P_{in} = 0.11$ mW. Then, by increasing the optical

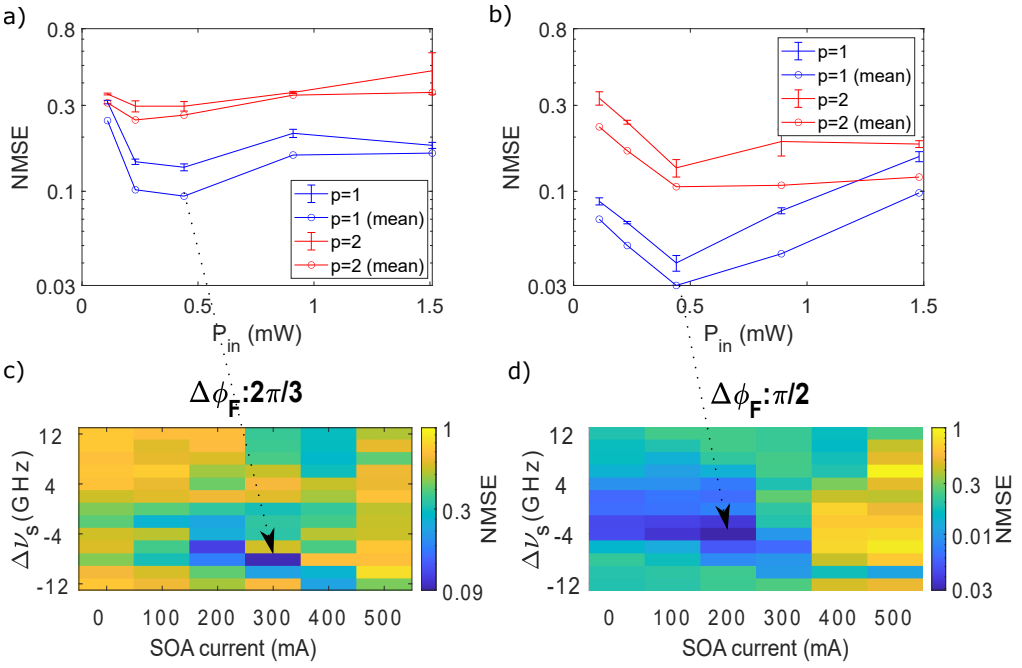

Fig. 7. Summary of the best NMSE performances obtained when varying the input optical power, in the a) Santa Fe, and b) Mackley Glass prediction tasks, respectively. Mapping of the $\Delta\nu_s$-SOA current parameter space where the best NMSE performance is found for a) the Santa Fe, and b) the Mackey Glass task, respectively. Here, an asynchronous encoding (k=1) is used. $\theta_v = 11$ ns, $N_v = 7$, $\tau_F = 88ns$. The dotted arrows point to the points in the map where the best NMSE values are achieved. Note that the NMSE is shown in a logarithmic scale in all figures.

Optics EXPRESS

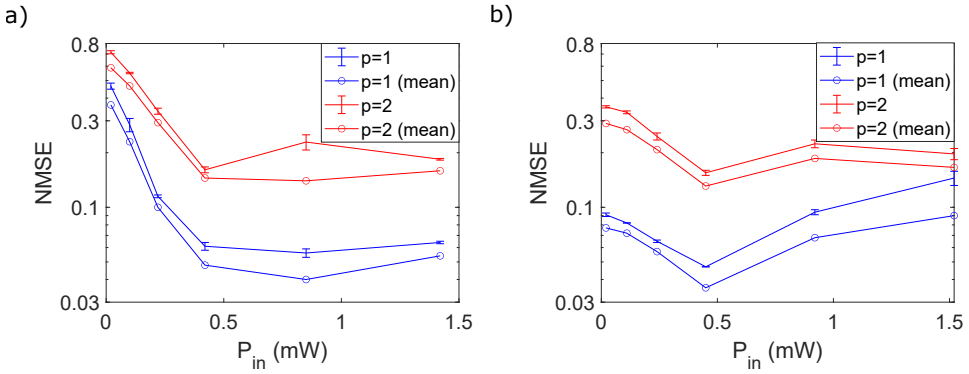

Fig. 8. Summary of the best NMSE performances obtained when varying the input optical power, in the absence of the feedback loop. The results refer to the a) Santa Fe and b) Mackley Glass prediction tasks, and are obtained using a much larger reservoir, with $\theta_v = 30$ ns, $b_w = 1140$ ns, and $N_v = 38$.

power, the system response becomes gradually shaped by the free carrier nonlinear dynamics, until self-pulsation dynamics appear for the highest optical power values [25].

An overview of the obtained performance for the Santa Fe and Mackey Glass prediction tasks are shown in Fig. 7(a-b), respectively, reporting the lowest NMSE in the parameter space ($\Delta\nu_s$, η_F, $\Delta\phi_F$) when varying the input optical power. Both 1-step ($p = 1$) and 2-step ($p = 2$) ahead prediction tasks are evaluated. In these tasks, we also compute the NMSE by averaging first the three optical trace repetitions and then estimating a unique NMSE (with no error, and labeled with 'mean' in the corresponding graphs). In general, increasing the input optical power turns out to be critical for both tasks, leading to the lowest $NMSE = 0.094$ in the Santa Fe task, and $NMSE = 0.03$ in the Mackey Glass task, when predicting the 1-step ahead value. The best results are obtained at the same input optical power $P_{in} = 0.44$ mW. The impact of the optical feedback contribution is critical, as we can observe from the corresponding parameter space $\Delta\nu_s$-SOA current for which we obtain this best performance (Fig. 7(c-d)). An SOA current around 300 mA and a phase condition of $\Delta\phi_F = 2\pi/3$ are required for the Santa Fe task, while an SOA current around 200 mA and a phase condition of $\Delta\phi_F = \pi/2$ are required to reach this performance for the Mackey Glass task. In both cases, the nonlinearly operating microring is coupled to a properly tuned optical feedback to provide the best performance on these tasks.

For the investigated tasks, it is unconventional to solve them with such low-dimensional expansion of the encoded sequence. Typically, other physical architectures that employ time delay RC use hundreds of virtual nodes [8]. For this reason, we consider now a longer external feedback loop and investigate what improvement this could bring to our previous results. To accommodate this larger number of virtual nodes, the feedback optical fiber is extended to provide a new delay time $\tau_F' = 1170$ ns (previously $\tau_F = 88$ ns). An asynchronous encoding is again applied with the input bit and the delayed bit mismatched by one virtual node separation time ($\tau_F' - b_w = \theta_v$). Specifically, we set $b_w = 1140$ ns and $\theta_v = 30$ ns, resulting in $N_v = b_w/\theta_v = 38$ virtual nodes.

The condition $\theta_v < \tau_{fc}$ still holds, which means that the microring nonlinear dynamics is still exploited as a coupling mechanism of neighboring virtual nodes. The NMSE values obtained for these new conditions and $N_v = 38$ virtual nodes are plotted versus the input optical power in Fig. 8(a-b) for the Santa Fe and Mackey Glass prediction tasks, respectively. The input optical power plays a critical role in both tasks also in this case. Note that, all the best performances obtained are for zero biasing currents of the SOA, thus in the absence of optical feedback. This is attributed to experimental issues related to the control of the phase in the long fiber loop. Therefore, the results in Fig. 8(a-b) show the performances of the microring resonator

Optics EXPRESS

without the feedback loop. The best performance achieved in the Santa Fe task (Fig. 8(a)) is $NMSE = 0.04$ when the target is one step ahead and at $P_{in} = 0.85$ mW. This value is lower than the one previously obtained with $N_v = 7$ virtual nodes (Fig. 7(a)). The best performance in the Mackey Glass task (Fig. 8(b)) is $NMSE = 0.036$, when the target is one step ahead and $P_{in} = 0.45$ mW. This error is instead larger than the one obtained with $N_v = 7$ virtual nodes (Fig. 7(b)), showing that the feedback loop is more critical for this task than for the Santa Fe one as already theoretically found in [27].

5. Discussion

5.1. Microring nonlinear memory

The results presented in the previous section show that a single microring without the external optical feedback can solve the Santa Fe and Mackey Glass prediction tasks. The memory needed to solve the task no longer relies on feedback echoes, but rather on the microring nonlinearity inertia. To validate this, we performed the following study. We set the microring operation with the optimal configurations found in the absence of feedback, and repeat the task by setting different separation times b_s between neighboring input optical pulses. If the separation time is large enough, the free carrier and temperature variations induced in the microring waveguide, when encoding the optical input x_i, will relax completely before the next optical pulse x_{i+1} is injected. Thus no trace of the previous information is stored in the microring when the next optical pulse propagates through it. Two examples of optical input pulses separated by $b_s = 0.21$ µs and $b_s = 0.6$ µs are considered and shown in Fig. 9(a). The red curves show the encoded pulses (without showing here the masking pre-processing) and the blue curves show the response of the microring at the drop port. For this study, we use the Santa Fe one-step-ahead ($p = 1$) prediction task. The system is first configured with the parametrization that leads to the best performance in Fig. 8(a): $P_{in} = 0.85$ mW, $\Delta\nu_s = 0$ GHz (not shown), no optical feedback. The virtual node separation time is $\theta_v = 30$ ns and the bit width is $b_w = 1140$ ns. Then, we solve the task for different input separation times b_s, as shown in Fig. 9(a).

The correspondent NMSE results versus b_s are shown in Fig. 9(b). We observe that the lowest NMSE value is preserved as long as two input optical pulses are close enough in time. For example, these are the cases of $b_s = 0$ and $b_s = 0.21$ µs. The performance is strongly degraded for larger b_s values. This time may be linked to both the slow decay rate of the free carrier population, and the longer thermal lifetime τ_{th} [33]. Indeed, the system's parameters ($\Delta\nu_s = 0$ GHz, $P_{in} = 0.85$ mW) used in the experiment excite self-pulsation dynamics (Fig. 9(a, blue curve)), which involves a competition of both free carrier and thermal effects. This dynamics is exploited to successfully obtain the lowest error (when b_s<0.21 µs). Under such dynamics, neighboring virtual nodes responses $N_{j,i}$ and $N_{j+1,i}$, for an input encoding x_i, are coupled using the spiking dynamics. In contrast, the responses of the same virtual node for neighboring input bits $N_{j,i}$ and $N_{j,i+1}$ are also coupled by a long-term memory given by the slow decay rate of the free carrier population and the longer thermal lifetime. Notably, this memory mechanism works only when an optical signal is propagating in the microring. This is ensured by operating the Mach Zehnder modulator in the linear regime of its transfer function, therefore having input information $x_i \approx 0$ encoded in a positive optical signal.

5.2. Variation of the number of virtual nodes

Without the limitation imposed by the external feedback loop length, we can select the input information duration b_w, and the number of virtual nodes $N_v = b_w/\theta_v$ in a more relaxed condition. Here, we investigate the impact of different reservoir sizes on the performance of the Santa Fe one-step-ahead prediction task. The number of virtual nodes N_v is tuned by keeping the same virtual node separation and stretching the bit width according to $b_w = \theta_v N_v$. In this case, the

Optics EXPRESS

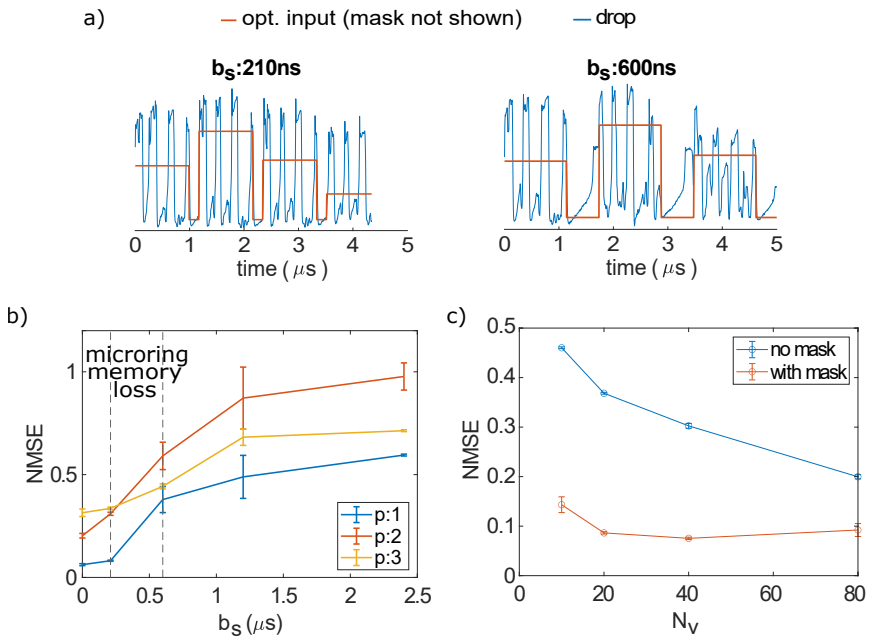

Fig. 9. Computation of the Santa Fe one step ahead prediction task, when considering a) two different separation times between encoded information b_s = 0.21 µs and b_s = 0.6 µs (red line, mask not shown). The corresponding output spiking dynamics are shown with blue lines. b) NMSE dependence on the input bit separation b_s, when considering N_v = 38 and θ_v = 30 ns. c) NMSE dependence on the number of virtual nodes $N_v = b_w/\theta_v$, which is tuned by changing the bit width b_w and keeping the same θ_v.

NMSE variations are dependent only on the number of virtual nodes N_v. The number of virtual nodes could also be tuned by keeping the same b_w and varying θ_v. Nevertheless, this last strategy would modify the nonlinear microring dynamics, thus the coupling between the virtual nodes. We operate the microring in the best-found configuration when defining 38 virtual nodes: $\Delta\nu_s = 0$, P_{in} = 0.85 mW, with an input encoded at θ_v = 30 ns, and b_s = 0 ns. This configuration, as it was shown in section 5.1, introduces memory in the system via the microring nonlinearity. We show the results in Fig. 9(c, red line), where we plot the NMSE obtained versus the number of virtual nodes N_v. A larger number of virtual nodes leads to NMSE reduction, until a saturation point. In Fig. 9(c, blue line), we show also the results achieved by turning off the input mask modulation. This is done since the microring undergoes self-pulsation dynamics (Fig. 9(a, blue curve)) when in a nonlinear regime. Thus, the virtual nodes $N_{j,i}$ response to an input pulse x_i are coupled by the microring spiking dynamics, which allows their state to experience a wide dynamical range: from a maximum value (spike's maximum peak) to a minimum value (valley between two spikes during the microring refractory period). Thus the masking procedure, which also aims at enriching the variability between virtual node states, may be not necessary, leading to a consequent simplification of the computing system. Experiments show that the masking is critical when using a small number of virtual nodes, and allows reaching the lowest NMSE already at N_v = 40. On the other hand, the benefit of masking becomes less relevant for a large number of virtual nodes. Due to hardware limitations in our system, related to the encoding of information and the memory of the instrumentation, we could not increase further N_v and verify the impact of the mask omission on the NSME values. Nevertheless, these observations

Optics EXPRESS

suggest that the mask could be replaced by the self-pulsation dynamics at the cost of a lower computational speed.

5.3. Performance comparison

Other works that consider a microring without optical feedback have reported error-free operation in delayed boolean tasks, but only considering up to 1 past bit ($d = 1$), relying on the information carried by the inertia of the free carrier [25,26] and thermal [47] nonlinearities. Here, we have shown experimentally that a linearly operating microring coupled with external optical feedback can solve delayed boolean tasks with up to $d = 3$ bits of memory. In particular, the XOR task is solved here for up to $d = 2$ bits, while it was shown in the literature to be solved with $d = 1$. For example, the XOR-1 task is solved in [48] using an integrated reservoir made of 16 microring resonators coupled in a swirl topology, in [43] using an integrated reservoir made only of combiners and splitters, and in [23] with an integrated SOA coupled to a feedback loop operated in a time delay RC approach. The XOR-2 is solved only in [43] using a parallel readout from several nodes in the network.

For solving analog prediction tasks, such as the Santa Fe and Mackey Glass time series prediction tasks, the contribution of the microring nonlinearities becomes important. The dynamical responses obtained at the output are shaped by the free carrier nonlinearity, or its interaction with the temperature nonlinearity (self-pulsations). In Table 2 we compare the performance obtained for the Santa Fe one-step ahead prediction task with other experimental time delay RC implementations. Our system in this table is classified as an optoelectronic (OE) implementation, due to the phase controller system, which also allows us to indirectly set the interference condition at the drop port by adjusting the feedback phase.

Table 2. Experimental time delay RC implementations tested on the Santa Fe benchmark task.[a]

Type	node	asynch.	feedback	N_V	θ_v	R	NMSE-1	NMSE-2	Ref.
OE	MZ	k=0	SMF	400	52.18ns	1	0.124	/	[11]
AO	DBF	k=0	WG + EM	6	40ps	1	0.423	/	[22]
AO	DBF	k=0	WG + EM	124	10ps	5	0.086	0.3	[22]
AO	SL	k=0	SMF	388	200ps	1	0.106	/	[20]
AO	SL	k=0	WG	23	50ps	1	0.135	/	[23]
AO	SL	k=0	WG	92	25ps	2	0.049	/	[23]
OE	SMR	k=1	SMF	7	11ns	1	0.094	0.249	our work
AO	SMR	/	/	38	30ns	1	0.04	0.14	our work

[a]OE: Optoelectronic; AO: All-optical; MZ: Mack Zehnder interferometer; DBF: Distributed feedback semiconductor laser; SL: Semiconductor laser; SMF: Single Mode Fiber; WG: Waveguide; EM: External mirror; SMR: Silicon microring; R: number of bit responses from which virtual nodes are sampled; NMSE-1(2): performance error when predicting the 1(2) step ahead time series value.

In some of the works of Table 2 [22,23], an increased number of virtual nodes is defined via post-processing techniques. This can be easily done by sampling in a time interval $R \cdot b_w$, with $R \in \mathbb{Z}^+$. Thus, instead of considering the response to only the present bit ($R = 1$, like it was done in this work), the virtual nodes sampling extends to more past responses ($R>1$), while keeping the same virtual node separation θ_v. This strategy introduces external memory to the classifier, by introducing some latency, which is not provided by the physical system. The value of R is also reported in Table 2. Many implementations report an NMSE calculated from the average optical response over several measurements, while in this work we estimate its mean value over only three repetitions. Nevertheless, the performances obtained by our configuration with only $N_v = 7$ virtual nodes and an optical feedback can be compared with implementations

Optics EXPRESS

that employ hundreds of nodes or that exploit external memory (R>1). Thus our results argue the common assumption that such prediction tasks require a large number of nodes to be solved. In the absence of optical feedback, the single microring with N_v = 38 virtual nodes, when operating in a self-pulsation dynamical regime, is able to provide the lowest prediction error compared to the implementations reported in Table 2.

Our implementation requires a dedicated phase controller to handle environmental noise, like in the case of [24]. Additionally, our current implementation has a processing speed limitation ($B_r = 1/(\theta_v N_v)$) that originates from the microring's free carrier nonlinearity (τ_{fc} = 45 ns). The time delay RC approach requires thus to define virtual node separation times of the same order, to effectively operate the reservoir under transient dynamics. Thus, the θ_v values used in our work are relatively high, even more than two orders of magnitude longer when compared to other implementations (Table 2). Nevertheless, the free carrier nonlinearity can be reduced to the *ps* scale with other fabrication approaches that exploit reversed bias pn junction [49], or graphene-on-silicon microrings for passive spiking emission up to 40 GHz [50]. In those cases, the feedback loop can be integrated to overcome the active control of the environmental phase noise that is needed for fiber-based configurations. It would also increase the overall computational speed of the system. Considering the benefit of using such a reduced number of virtual nodes, the overall trade-off enables us to believe that this concept for reservoir computing can have competitive attributes against the existing demonstrations.

6. Conclusions

Silicon microrings, with their passive dynamics, offer promising prospects for time-delay reservoir computing and neuromorphic computation, making them strong candidates for future integrated photonic implementations that can synergize with other strategic elements. Our experimental study demonstrates their versatility in extending the system's memory by introducing external optical feedback. We reveal the computational potential of microring resonators in such a configuration by achieving error-free operation for delayed boolean tasks up to 3 bits in the past. We also show competitive results in complex tasks like the Mackey Glass and Santa Fe tasks when defining a photonic reservoir with a very small number (7) of virtual nodes. This finding promotes the usefulness of working with small-scale networks, such as an integrated version of our system, for solving prediction tasks. It extends even further to various hardware architectures with different real nodes, and complements similar findings recently reported on classification tasks [51]. Furthermore, we report best-in-class performance in the Santa Fe task by leveraging self-pulsation dynamics. This approach, not previously explored for these applications, offers new insights into memory dynamics.

Appendix: Operation of the phase controller

The successful implementation of the system for time delay RC relies on the phase controller developed to compensate for environmental thermal, phonic, and vibrational noise. The drop signal, is the result of the interference between the optical field from the microring (R) and the field from the feedback loop (F), as represented in Fig. 10(a). These two fields can be expressed in a simple way that highlights their relative phase as $R = A$ and $F = Be^{i\Delta\phi_F}$. As a result, the optical power at the drop port is:

$$|R + F|^2 = A^2 + B^2 + 2ABcos(\Delta\phi_F), \tag{3}$$

and ranges between maximum and minimum identified by $A^2 + B^2 \pm 2AB$. The amplitude of the two field components defines the interference range, while the relative phase states the interference condition at the drop port: constructive ($\Delta\phi_F = 0$), destructive ($\Delta\phi_F = \pi$), or intermediate, with a π-periodicity. Environmental noise randomly changes the phase of the delayed signal and is

Optics EXPRESS

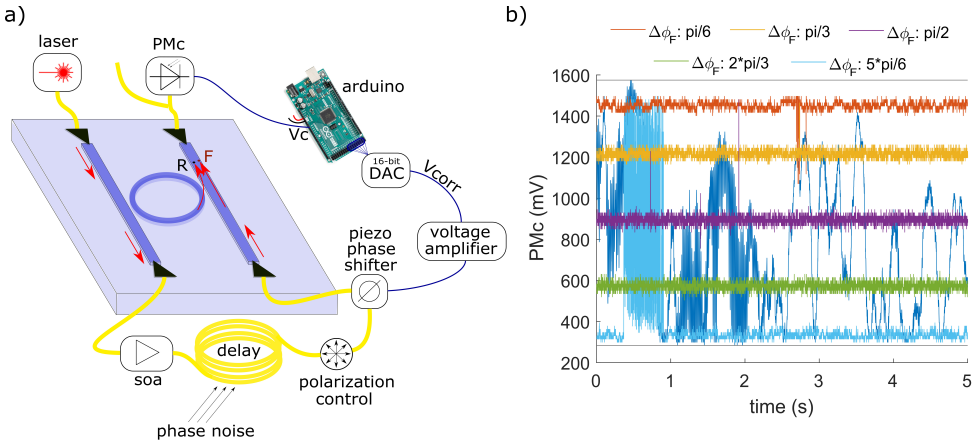

Fig. 10. a) An Arduino-based controller stabilizes the system against environmental noise accumulated along the feedback loop (τ_F = 88 ns). 'R' and 'F' refer to the optical components from the ring and the feedback, respectively, that contribute to the drop signal. b) The microring's drop response to a CW input, as monitored by the slow photodetector PM_c. The deep-blue curve in the background is the interference signal without any phase stabilization. The rest colored lines represent the stabilized signal via the Arduino-based controller, for different phase conditions.

thus included in Eq. (3), as fluctuations of the $\Delta\phi_F$ values over time. As a result, the drop signal, which is driven by this noise, randomly varies within the interference intensity range, even when a continuous wave (CW) input signal is injected into the system, as shown in Fig. 10(b, blue background line). This noise is compensated by properly driving the piezo phase shifter that is incorporated in the feedback line. To do so while performing the task, we detect the interference signal with a 3-kHz bandwidth photodetector at the drop port (PM_c). Then, we set the desired phase condition at the drop port, $\Delta\phi_F$, by computing the corresponding optical power via Eq. (3). A phase target close to the interference limits ($\Delta\phi_F = 0$ and $\Delta\phi_F = \pi$) is not optimal, since noisy shifts of the interference can easily bring the correspondent optical target out of range and cause correction fails. For this reason, $\Delta\phi_F$ has been slightly restricted in the range $[\pi/6 - 5\pi/6]$ when performing the tasks, limiting correction fails to only strong perturbations, like vibrations of the optical table, as shown in Fig. 10(b) (see the $\Delta\phi_F = 5\pi/6$ curve).

For the operation of the Arduino Mega, we initially set a reference target value (v_{tar}). The Arduino controller in each iteration step compares v_{tar} with the signal obtained by the slow photodetector PM_c (v_c) and estimates an error $err = v_{tar} - v_c$. Finally, similarly to a PID controller, it elaborates a correction signal $v_{corr} = (v_{corr} + (k_p * err))$, by changing the proportional term, with constant k_p. This signal is sent to a voltage amplifier and then used to drive the phase shifter. The Arduino controller updates the correction every 55 µs approximately, thus at 18 kbps. However, the voltage amplifier used in this setup has only 200 Hz bandwidth, limiting the effective speed of the control system. Still, the controller is able to suppress almost entirely the environment noise, as shown by the stabilized traces of the output at the drop port, for different $\Delta\phi_F$ values (Fig. 10(b)). The stabilization is achieved without any further isolation of the system from the environment.

Funding. Ministerio de Ciencia e Innovación (CEX2021-001164-M (Maria de Maeztu Project), MCIN/AEI/10.13039/501100011033); H2020 European Research Council (788793, BACKUP).

Acknowledgments. The authors thank Riccardo Franchi, Davide Bazzanella, and Stefano Biasi for the technical help and fruitful discussions. The authors also acknowledge the support by the María de Maeztu project CEX2021-001164-M funded by the MCIN/AEI/10.13039/501100011033.

Optics EXPRESS

Disclosures. The authors declare that there are no conflicts of interest related to this article.

Data availability. Data underlying the results presented in this paper are not publicly available at this time but may be obtained from the authors upon reasonable request.

References

1. C. D. Schuman, S. R. Kulkarni, M. Parsa, *et al.*, "Opportunities for neuromorphic computing algorithms and applications," Nat. Comput. Sci. **2**(1), 10–19 (2022).
2. A. Mehonic and A. J. Kenyon, "Brain-inspired computing needs a master plan," Nature **604**(7905), 255–260 (2022).
3. G. Giamougiannis, A. Tsakyridis, M. Moralis-Pegios, *et al.*, "Universal linear optics revisited: new perspectives for neuromorphic computing with silicon photonics," IEEE J. Sel. Top. Quantum Electron. **29**(2: Optical Computing), 1–16 (2022).
4. B. J. Shastri, A. N. Tait, T. Ferreira de Lima, *et al.*, "Photonics for artificial intelligence and neuromorphic computing," Nat. Photonics **15**(2), 102–114 (2021).
5. W. Maass, T. Natschläger, and H. Markram, "Real-time computing without stable states: A new framework for neural computation based on perturbations," Neural computation **14**(11), 2531–2560 (2002).
6. H. Jaeger, "The "echo state" approach to analysing and training recurrent neural networks-with an erratum note," Bonn, Germany: German National Research Center for Information Technology GMD Technical Report 148, 13 (2001).
7. C. Fernando and S. Sojakka, "Pattern recognition in a bucket," in *Advances in Artificial Life: 7th European Conference, Proceedings 7* (Springer, 2003), pp. 588–597.
8. L. Appeltant, M. C. Soriano, G. Van der Sande, *et al.*, "Information processing using a single dynamical node as complex system," Nat. Commun. **2**(1), 468 (2011).
9. D. Brunner, B. Penkovsky, B. A. Marquez, *et al.*, "Tutorial: Photonic neural networks in delay systems," J. Appl. Phys. **124**(15), 152004 (2018).
10. Y. Paquot, F. Duport, A. Smerieri, *et al.*, "Optoelectronic reservoir computing," Sci. Rep. **2**(1), 287 (2012).
11. L. Larger, M. C. Soriano, D. Brunner, *et al.*, "Photonic information processing beyond turing: an optoelectronic implementation of reservoir computing," Opt. Express **20**(3), 3241–3249 (2012).
12. M. Abdalla, C. Zrounba, R. Cardoso, *et al.*, "Minimum complexity integrated photonic architecture for delay-based reservoir computing," Opt. Express **31**(7), 11610–11623 (2023).
13. S. Ortin, M. C. Soriano, L. Pesquera, *et al.*, "A unified framework for reservoir computing and extreme learning machines based on a single time-delayed neuron," Sci. Rep. **5**(1), 14945 (2015).
14. F. Duport, B. Schneider, A. Smerieri, *et al.*, "All-optical reservoir computing," Opt. Express **20**(20), 22783–22795 (2012).
15. R. M. Nguimdo, G. Verschaffelt, J. Danckaert, *et al.*, "Simultaneous computation of two independent tasks using reservoir computing based on a single photonic nonlinear node with optical feedback," IEEE Trans. Neural Netw. Learning Syst. **26**(12), 3301–3307 (2015).
16. J. Bueno, D. Brunner, M. C. Soriano, *et al.*, "Conditions for reservoir computing performance using semiconductor lasers with delayed optical feedback," Opt. Express **25**(3), 2401–2412 (2017).
17. A. Argyris, J. Bueno, and I. Fischer, "Photonic machine learning implementation for signal recovery in optical communications," Sci. Rep. **8**(1), 8487 (2018).
18. A. Argyris, J. Bueno, and I. Fischer, "Pam-4 transmission at 1550 nm using photonic reservoir computing post-processing," IEEE Access **7**, 37017–37025 (2019).
19. I. Estébanez, S. Li, J. Schwind, *et al.*, "56 gbaud pam-4 100 km transmission system with photonic processing schemes," J. Lightwave Technol. **40**(1), 55–62 (2021).
20. D. Brunner, M. C. Soriano, C. R. Mirasso, *et al.*, "Parallel photonic information processing at gigabyte per second data rates using transient states," Nat. Commun. **4**(1), 1364 (2013).
21. J. Bueno, J. Robertson, M. Hejda, *et al.*, "Comprehensive performance analysis of a vcsel-based photonic reservoir computer," IEEE Photonics Technol. Lett. **33**(16), 920–923 (2021).
22. K. Takano, C. Sugano, M. Inubushi, *et al.*, "Compact reservoir computing with a photonic integrated circuit," Opt. Express **26**(22), 29424–29439 (2018).
23. K. Harkhoe, G. Verschaffelt, A. Katumba, *et al.*, "Demonstrating delay-based reservoir computing using a compact photonic integrated chip," Opt. Express **28**(3), 3086–3096 (2020).
24. Q. Vinckier, F. Duport, A. Smerieri, *et al.*, "High-performance photonic reservoir computer based on a coherently driven passive cavity," Optica **2**(5), 438–446 (2015).
25. M. Borghi, S. Biasi, and L. Pavesi, "Reservoir computing based on a silicon microring and time multiplexing for binary and analog operations," Sci. Rep. **11**(1), 15642 (2021).
26. D. Bazzanella, S. Biasi, M. Mancinelli, *et al.*, "A microring as a reservoir computing node: memory/nonlinear tasks and effect of input non-ideality," J. Lightwave Technol. **40**(17), 5917–5926 (2022).
27. G. Donati, C. R. Mirasso, M. Mancinelli, *et al.*, "Microring resonators with external optical feedback for time delay reservoir computing," Opt. Express **30**(1), 522–537 (2022).
28. S. Biasi, G. Donati, A. Lugnan, *et al.*, "Photonic neural networks based on integrated silicon microresonators," arXiv arXiv:2306.04779 (2023).

Optics EXPRESS

29. A. N. Tait, M. A. Nahmias, B. J. Shastri, *et al.*, "Broadcast and weight: an integrated network for scalable photonic spike processing," J. Lightwave Technol. **32**(21), 4029–4041 (2014).
30. A. N. Tait, T. F. De Lima, E. Zhou, *et al.*, "Neuromorphic photonic networks using silicon photonic weight banks," Sci. Rep. **7**(1), 7430 (2017).
31. C. Huang, S. Fujisawa, T. F. de Lima, *et al.*, "A silicon photonic–electronic neural network for fibre nonlinearity compensation," Nat. Electron. **4**(11), 837–844 (2021).
32. M. Hejda, E. A. Doris, S. Bilodeau, *et al.*, "Interfacing spiking vcsel-neurons with silicon photonics weight banks towards integrated neuromorphic photonic systems," arXiv arXiv:2305.00788 (2023).
33. M. Borghi, D. Bazzanella, M. Mancinelli, *et al.*, "On the modeling of thermal and free carrier nonlinearities in silicon-on-insulator microring resonators," Opt. Express **29**(3), 4363–4377 (2021).
34. V. R. Almeida and M. Lipson, "Optical bistability on a silicon chip," Opt. Lett. **29**(20), 2387–2389 (2004).
35. T. J. Johnson, M. Borselli, and O. Painter, "Self-induced optical modulation of the transmission through a high-q silicon microdisk resonator," Opt. Express **14**(2), 817–831 (2006).
36. G. Priem, P. Dumon, W. Bogaerts, *et al.*, "Optical bistability and pulsating behaviour in silicon-on-insulator ring resonator structures," Opt. Express **13**(23), 9623–9628 (2005).
37. S. Chen, L. Zhang, Y. Fei, *et al.*, "Bistability and self-pulsation phenomena in silicon microring resonators based on nonlinear optical effects," Opt. Express **20**(7), 7454–7468 (2012).
38. M. Mancinelli, M. Borghi, F. Ramiro-Manzano, *et al.*, "Chaotic dynamics in coupled resonator sequences," Opt. Express **22**(12), 14505–14516 (2014).
39. A. Argyris, J. Schwind, and I. Fischer, "Fast physical repetitive patterns generation for masking in time-delay reservoir computing," Sci. Rep. **11**(1), 6701 (2021).
40. F. Duport, A. Smerieri, A. Akrout, *et al.*, "Fully analogue photonic reservoir computer," Sci. Rep. **6**(1), 22381 (2016).
41. T. Hülser, F. Köster, L. Jaurigue, *et al.*, "Role of delay-times in delay-based photonic reservoir computing," Opt. Mater. Express **12**(3), 1214–1231 (2022).
42. M. Inubushi and K. Yoshimura, "Reservoir computing beyond memory-nonlinearity trade-off," Sci. Rep. **7**(1), 10199 (2017).
43. K. Vandoorne, P. Mechet, T. Van Vaerenbergh, *et al.*, "Experimental demonstration of reservoir computing on a silicon photonics chip," Nat. Commun. **5**(1), 3541 (2014).
44. A. S. Weigend and N. A. Gershenfeld, "Results of the time series prediction competition at the Santa Fe institute," in *International conference on neural networks* (IEEE, 1993), pp. 1786–1793.
45. M. C. Mackey and L. Glass, "Oscillation and chaos in physiological control systems," Science **197**(4300), 287–289 (1977).
46. H. Jaeger and H. Haas, "Harnessing nonlinearity: Predicting chaotic systems and saving energy in wireless communication," Science **304**(5667), 78–80 (2004).
47. G. Donati, "A time-delay reservoir computing neural network based on a single microring and external optical feedback," Ph.D. thesis, University of Trento and University of the Balearic Islands (2023).
48. F. Denis-Le Coarer, M. Sciamanna, A. Katumba, *et al.*, "All-optical reservoir computing on a photonic chip using silicon-based ring resonators," IEEE J. Sel. Top. Quantum Electron. **24**(6), 1–8 (2018).
49. S. F. Preble, Q. Xu, B. S. Schmidt, *et al.*, "Ultrafast all-optical modulation on a silicon chip," Opt. Lett. **30**(21), 2891–2893 (2005).
50. A. Jha, C. Huang, H.-T. Peng, *et al.*, "Photonic spiking neural networks and graphene-on-silicon spiking neurons," J. Lightwave Technol. **40**(9), 2901–2914 (2022).
51. S. Biasi, R. Franchi, L. Cerini, *et al.*, "An array of microresonators as a photonic extreme learning machine," APL Photonics **8**(9), 096105 (2023).